2007-01-16

Intersubject Regularity in the Intrinsic Shape of Human V1

Intersubject regularity in the intrinsic shape of human V1

Oliver P. Hinds[1], Jonathan R. Polimeni[2,3], Niranjini Rajendran[3], Mukund Balasubramanian[1], Lawrence L. Wald[3], H. Diana Rosas[4], Matthew P. Frosch[5,6], Jean C. Augustinack[3], GrahamWiggins[3], Andreas Potthast[7], Bruce Fischl[3,8], and Eric L. Schwartz[1,2,9]

1Department of Cognitive and Neural Systems, Boston University
2Department of Electrical and Computer Engineering, Boston University
3Department of Radiology, MGH, Athinoula A. Martinos Center, Harvard Medical School
4Department of Neurology, MGH, Athinoula A. Martinos Center, Harvard Medical School
5MassGeneral Institute for Neurodegenerative Disease, Department of Neurology, MGH
6C.S. Kubik Laboratory for Neuropathology, Department of Pathology, MGH
7Siemens Medical Solutions, Inc, Malvern, PA USA
8Computer Science and Artificial Intelligence Laboratory, Massachusetts Institute of Technology
9Department of Anatomy and Neurobiology, Boston University School of Medicine

Submitted January 16, 2007
CAS/CNS Technical Report 2007-002

Abstract

Previous studies have reported considerable intersubject variability in the three-dimensional geometry of the human primary visual cortex (V1). Here we demonstrate that much of this variability is due to extrinsic geometric features of the cortical folds, and that the *intrinsic* shape of V1 is similar across individuals. V1 was imaged in ten *ex vivo* human hemispheres using high-resolution (200 μm) structural magnetic resonance imaging at high field strength (7 T). Manual tracings of the stria of Gennari were used to construct a surface representation, which was computationally flattened into the plane with minimal metric distortion. The intrinsic shape of V1 was determined from the boundary of the planar representation of the stria. An ellipse provided a simple parametric shape model that was a good approximation to the boundary of flattened V1. The aspect ratio of the best-fitting ellipse was found to be consistent across subjects, with a mean of 1.85 and standard deviation of 0.12. Optimal rigid alignment of size-normalized V1 produced greater overlap than that achieved by previous studies using different registration methods. A shape analysis of published macaque data indicated that the intrinsic shape of macaque V1 is also stereotyped, and similar to the human V1 shape. Previous measurements of the functional boundary of V1 in human and macaque are in close agreement with these results.

The human primary visual cortex (V1) is a readily identifiable architectonic area containing a complete topographic representation of the contralateral visual hemifield. The stria of Gennari—a thin band of heavily myelinated tissue in cortical layer IVCα (Boyd and Matsubara, 2005)—provides an anatomical landmark delineating V1, which is also known as striate cortex. Previously, magnetic resonance imaging (MRI) of the stria has been used to identify V1 (Clark et al., 1992; Barbier et al., 2002; Fatterpekar et al., 2002; Walters et al., 2003; Bridge et al., 2005), but in prior studies the full cortical area has not been imaged.

The cortex is well-approximated as a two-dimensional sheet embedded in three-dimensional Euclidean space. The geometry of the cortical surface consists of intrinsic factors—such as distances along the surface—that are by definition preserved under isometric transformations, as well as extrinsic factors—such as sulcal depth—that are not preserved (Griffin, 1994). Several studies have reported substantial variability in the geometric features of V1 (Brodmann, 1918; von Economo and Koskinas, 1925; Putnam, 1926; Popoff, 1927; Filimonov, 1932; Polyak, 1957; Stensaas et al., 1974; Roland et al., 1997; Amunts et al., 2000), but did not account for the substantial intersubject variability of the extrinsic geometric features of the cortex. By minimizing the impact of the extrinsic geometry we found that the intrinsic shape of V1 is much more similar across subjects than casual inspection suggests.

In the present study, high-resolution (≤ 200 μm) images of ten *ex vivo* human hemispheres were collected using MRI at 7 T field strength. Two-dimensional mesh representations of the full V1 surface were constructed from manual identifications of the stria in the MRI volumes. To perform quantitative analysis of the intrinsic geometric structure of V1, surfaces were mapped into the plane using a flattening algorithm that minimizes global metric distortion (Balasubramanian et al., 2005).

The aspect ratio of the ellipse that best fit the boundary of flattened V1 was computed, providing a geometric description of the intrinsic shape of V1 independent of overall size. A statistical analysis of the aspect ratio demonstrated a consistent V1 shape across subjects. As an independent measure of shape similarity, a size-normalized, rigid-body alignment of the V1 boundary was performed across subjects to determine the overlap and spread of V1 while preserving shape. Also, the average shape of human V1 was found to be very similar to that of macaque V1 based on a statistical shape analysis of published anatomical data (Horton and Hocking, 1996). Based on independent experiments that established similarity in the visuotopic mappings of these two species (Polimeni et al., 2005, 2006a), the similarity of the anatomical shape of V1 across subjects, as well as between human and macaque, was expected and is here confirmed.

Preliminary versions of this work have appeared in abstract form (Hinds et al., 2005a,b).

Materials and Methods

Magnetic resonance imaging

Ten whole, formalin fixed *ex vivo* human cerebral hemispheres were collected under an Institutional Review Board-approved protocol through the autopsy service of the Massachusetts General Hospital and with the cooperation of the Massachusetts Alzheimer Disease Research Center, the Massachusetts Eye and Ear Infirmary, and the Center for Neuroimaging of Aging and Neurodegenerative Disease. Seven of these hemispheres were from individuals with no history of neurological disease, while two were from individuals with Huntington's disease (HD), and one was from an individual with Alzheimer's disease (AD). The occipital lobe of each hemisphere was imaged using a head-only 7 T MR system based on either a Siemens MAGNETOM Sonata or a Siemens MAGNETOM Avanto platform (Siemens Medical Solutions, Erlangen, Germany). The imaging volume covered approximately the posterior third of the hemisphere, containing all of V1, as well as surrounding tissue in the occipital lobe.

The optimal pulse sequence parameters for gray and white matter contrast were determined by synthesizing T1-weighted, T2*-weighted, and proton density-weighted images from a volume acquired using a three-dimensional, multi-echo fast, low-angle shot (FLASH) pulse sequence (Fischl et al., 2004), and then analyzing the contrast-to-noise ratio between gray and white matter per unit time. Based on this analysis, low-bandwidth FLASH pulse sequence parameters were optimized for imaging the stria of Gennari in these *ex vivo* hemi-

spheres. Fixation of the hemispheres induced shortening of the T1 relaxation time for both gray and white matter, and disproportionately compressed the difference in relaxation time between the tissue types (Tovi and Ericsson, 1992; Pfefferbaum et al., 2004; Augustinack et al., 2005). Thus, the resulting MR images were predominantly T2*-weighted.

The voxel size was either 180 or 200 μm, and was isotropic with zero interslice distance. All acquisitions were collected with an echo time of 20 ms, a flip angle of 30°, and a bandwidth of 30 Hz per pixel. The low pixel bandwidth of this pulse sequence boosts the signal-to-noise ratio (SNR) within the small voxels, but increases imaging distortions. Geometric MRI distortions due to tissue susceptibility inhomogeneity and magnetic gradient nonlinearity were examined and found to be small compared to the thickness of gray matter, as discussed in the Supplementary Material. Depending on the properties of the particular radiofrequency (RF) coil and the size of the field of view (FOV), the length and number of acquisitions varied from three acquisitions at 4 h each to twelve acquisitions at 1 h 15 min each. The number of acquisitions required was determined by inspecting the resulting averaged volume for reliable visibility of the stria of Gennari. All RF coils used during imaging were custom designed and built. A four-channel surface coil and three different volume coils (Wald et al., 2005) were used to image hemispheres for the stria. The specific MRI parameters used for each hemisphere are shown in Table 1.

Table 1: MRI parameters used for each *ex vivo* hemisphere. Note that all hemispheres are from different individuals except for LH2 and RH2 and LH4 and RH4.

hemisphere	**gender**	**age**	**acquisitions**	**total time** (h)	**voxel size** (mm)	**FOV** (mm)	**repetition time** (ms)	**neurological disease**
LH1	M	79	11	13.8 h	$0.20 \times 0.20 \times 0.20$	100.00×75.00	40 ms	none
RH1	F	50	12	15.1 h	$0.20 \times 0.20 \times 0.20$	100.00×75.00	40 ms	none
LH2	M	81	3	12.2 h	$0.18 \times 0.18 \times 0.18$	115.00×115.00	43 ms	none
RH2	M	81	3	12.2 h	$0.18 \times 0.18 \times 0.18$	115.00×115.00	43 ms	none
LH3	NA	NA	6	9.8 h	$0.18 \times 0.18 \times 0.18$	69.43×81.00	40 ms	HD
RH3	NA	NA	10	15.2 h	$0.18 \times 0.18 \times 0.18$	57.50×138.00	41 ms	HD
LH4	F	75	5	10.5 h	$0.20 \times 0.20 \times 0.20$	102.00×102.00	42 ms	none
RH4	F	75	5	10.5 h	$0.20 \times 0.20 \times 0.20$	102.00×102.00	42 ms	none
LH5	M	80	4	9.4 h	$0.20 \times 0.20 \times 0.20$	76.80×128.00	43 ms	AD
RH5	NA	NA	9	14.7 h	$0.18 \times 0.18 \times 0.18$	69.43×81.00	40 ms	none

Ex vivo hemispheres were chosen over live subjects for imaging of the stria of Gennari for several reasons. The absence of the skull allows the small RF surface coils to be placed closer to the tissue of interest, thus boosting the SNR. In addition, Specific Absorption Rate restrictions limit the type and length of MRI acquisitions acceptable for use on live human subjects. Also, the long imaging times required for reliable detection of the stria in the MRI volumes were unacceptable for live subjects. Further, there is no overt, cardiac, or respiratory movement when imaging *ex vivo* hemispheres, although vibration of the scanner bed itself and RF heating of the hemispheres caused some movement over the long duration of the experiment. Motion correction (Jenkinson et al., 2002) was applied to the imaging volumes to correct for between acquisition hemisphere motion.

Identifying the stria of Gennari

Figure 1 shows an MR image typical of the data collected for this study, with the stria of Gennari clearly visible as a dark stripe through the lighter gray matter in V1. This stripe ends abruptly at the V1 boundary, providing a highly reliable myeloarchitectonic landmark delimiting V1 (Henschen, 1890; Bolton, 1900; Polyak, 1933; Clark, 1941). Only data in which the stria was visible throughout the full volume were used. In these data the profile of the stria was manually traced in the coronal plane of each hemisphere using custom software (Hinds et al., 2006) that aided the tracing of features in slice data.

Figure 1(C) shows the tracing of the stria identified in the slice shown in Figure 1(B). The result of the tracing process is a set of *slice contours*, each of which represents a single connected component of the intersection of the stria in three dimensions with the two-dimensional slice plane. The extensive folding of the

human occipital lobe is such that complicated branching of slice contours can occur between slices, and each contour can be either an open curve or a closed polygon—key challenges for existing surface reconstruction methods.

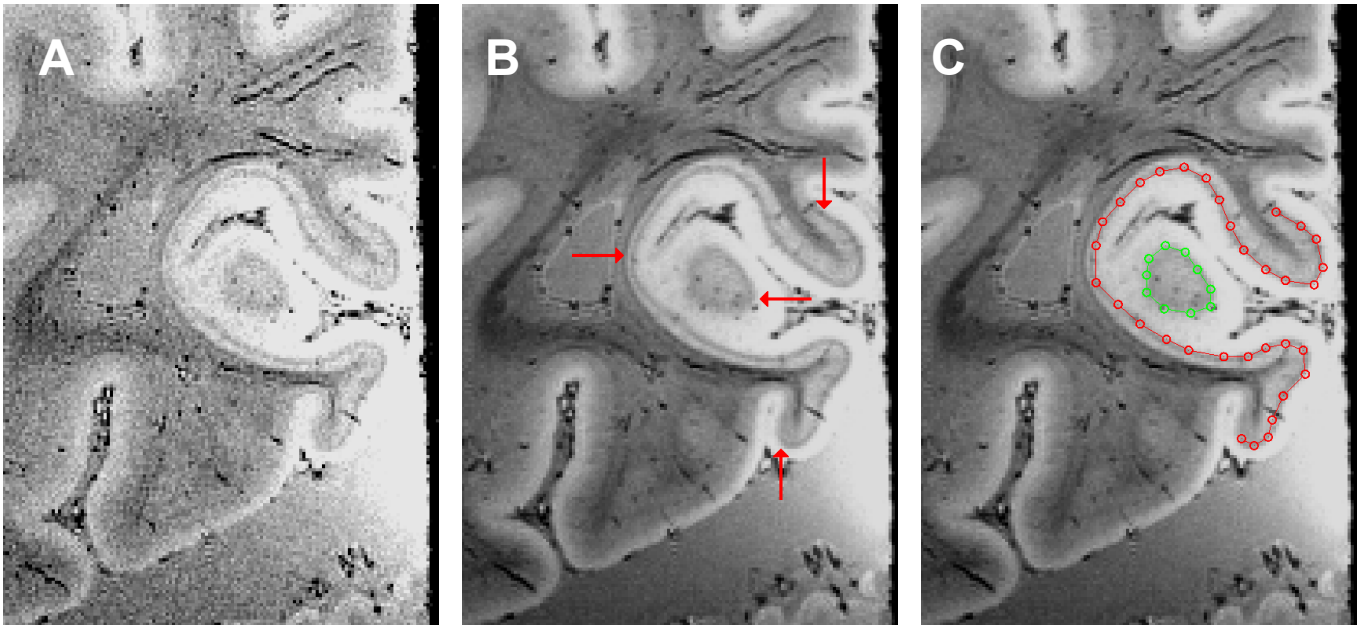

Figure 1: (A) An example coronal MR image from a single 99 min acquisition of hemisphere LH3. The isotropic voxel size for this image is 180 µm. (B) The same slice shown in (A) after seven acquisitions were motion corrected and averaged to achieve high contrast-to-noise ratio. The total imaging time for this hemisphere was about 11.5 h. The stria (red arrows) is plainly visible. (C) A tracing of the stria of Gennari in the same image shown in (B). The two colors represent two connected components of intersection of the striate surface with the MR slice plane. The red contour is open, the green contour is closed.

Surface reconstruction and flattening

Consistently reliable automatic segmentation of the stria was not feasible for this imaging data, and manual voxel labeling was not practical for the large amount of data used here. Therefore, contour tracing was used to identify the stria, but surface reconstruction from slice contours presents problems for commonly used surface meshing methods.

If voxels labeling the stria were available, isosurfacing methods, such as MARCHING CUBES (Lorensen and Cline, 1987), could be used directly to construct an accurate surface representation of V1. However, given a slice contour representation, isosurfacing methods require that a voxel-based representation be generated from the slice contours. This process yields surfaces with many errors when the contours are from complex surfaces, such as cerebral cortex (Meyers et al., 1992).

Methods specifically developed to reconstruct surfaces from slice contours, such as that presented by Boissonnat (1988), are not designed to reconstruct surfaces with boundaries (e.g., a topological disk) because they require the reconstructed surfaces to be closed (e.g., a topological sphere). Although contours can be artificially closed, these methods fail if closure of the slice contours results in self-intersections, which is the case for many V1 contours. To overcome these difficulties, we developed a new surface reconstruction algorithm that allows reconstruction of partial- or whole-brain surfaces from a slice contour representation. This algorithm accepts a set of slice contours as input and tiles one pair of adjacent slices at a time, concatenating the surfaces between each slice pair to obtain the entire surface. The details of the reconstruction algorithm have been presented in abstract form (Hinds et al., 2006). Both the graphical user interface used to trace the stria and the software used to reconstruct the V1 surfaces are available as part of a Surface Construction application downloadable from

http://eslab.bu.edu/software.

Every fourth slice was used to reconstruct the surface of the stria, providing an interslice interval of about 0.8 mm. Care is necessary when choosing the interslice interval because extremely large values undersample the surface, while extremely small values can introduce numerous small geometric errors in the surface representation. Therefore, undersampling or oversampling can lead to substantial error in surface area estimates, as discussed in the Supplementary Material.

Because the three-dimensional cortical surface has non-zero Gaussian curvature, it is impossible to isometrically map the surface of V1 into the plane (Do Carmo, 1976). In practice, it is possible to compute a least-squares optimal near-isometry by preserving the surface-based shortest-path distance for each vertex pair, resulting in a planar representation of the surface that matches the intrinsic geometry of the original surface as closely as possible (Balasubramanian et al., 2005). The V1 surfaces were near-isometrically flattened, and the error was computed as the difference between the shortest-path distances in the three-dimensional surface and the corresponding Euclidean distances in the two-dimensional surface. Using exact, global distances as opposed to nearest-neighbor distances, which are commonly employed, provides more accurate flat representations of the cortex (Balasubramanian et al., 2005, 2006).

Shape of V1

After flattening, the best fitting ellipse to the flattened boundary shape of V1 was computed by minimizing the residual root-mean-squared (RMS) error, E_{RMS}, between the boundary vertex coordinates and the ellipse. E_{RMS} is defined as

$$E_{\mathrm{RMS}} = \sum_{v} \left\| 1 - \left(\frac{v_x}{e_1}\right)^2 - \left(\frac{v_y}{e_2}\right)^2 \right\|,$$

where v_x and v_y are the two Cartesian coordinates of a V1 boundary vertex v, and e_1 and e_2 are the lengths of the semi-major and semi-minor ellipse axes, respectively. The aspect ratio e_1/e_2 of the best fitting ellipse was used as a measure of the intrinsic shape of V1 since it is independent of overall size. It is important to note that the ellipse only serves as a simple parametric description of the shape of the boundary of V1, without assuming any particular form for the topographic map, which would also provide a model for the shape of the V1 boundary. To assess the similarity of the intrinsic shape of V1 across subjects, the sample mean and standard deviation of the aspect ratio of the best fitting ellipse were computed.

As a further independent analysis of the intrinsic shape variability, rigid-body transformations were used to co-register the flattened V1 surfaces of each subject without assuming any model for the boundary shape. First, the global scale of each flattened V1 surface was discounted by normalizing the surface area. To compute the alignment of V1, the Iterative Closest Point (ICP) shape alignment method (Besl and McKay, 1992) was used to align the boundary vertices for each surface to those of a single subject, which provided a common planar reference space. The probability of observing V1 at each point in the reference space (i.e. a probability map) was computed.

After alignment, the similarity of the V1 surfaces was examined to assess the quality of registration. Two measures of similarity were used: *average percent overlap* (e.g., Nieto-Castanon et al., 2003) and *percent blurring* (e.g., Fischl et al., 1999). The average percent overlap $P_{\mathrm{o}}(R)$ is defined as

$$P_{\mathrm{o}}(R) = 100 \frac{1}{M_R} \sum_{j=1}^{M_R} \frac{\bigcap a_i}{\bar{a}_j} \tag{1}$$

for $R \in \{2,\ldots,N\}$ V1 surfaces in each combination, where $M_R = \binom{N}{R}$ is the number of combinations of the N V1 surfaces, $\bar{a}_j$ is the average area of the R surfaces in combination j, and $\bigcap a_i$ represents the area of the spatial intersection across the V1 surfaces in combination j, indexed by $i \in \{1,\ldots,R\}$.

The percent blurring statistic P_b is defined as

$$P_b = 100 \frac{\bigcup a_k - \bar{a}}{\bar{a}}, \tag{2}$$

where $\bar{a}$ is the average area of the V1 surfaces and $\bigcup a_k$ is the area of the spatial union of the V1 surfaces. Intuitively, the average percent overlap is the ratio of the area common to all V1 surfaces to the mean area of the surfaces, while the percent blurring relates the area of the total spread of V1 to the mean area.

Results

Three-dimensional V1 surfaces

The surface reconstruction of V1 for each of the hemispheres is shown in Figure 2. The extrinsic geometric features of the location, size, and folding pattern of V1 in these hemispheres vary substantially. In this population, the surface area of V1 varies by a factor of more than two, with a mean of 2960 ± 760 mm^2, as shown in Table 2. This variation is consistent with that found in other studies (Stensaas et al., 1974).

Shape of flattened V1

The flattening error across all samples was consistently low, with a mean of 5.8% and a standard deviation of 0.7%. The shape of flattened V1 for each hemisphere is shown beside its three-dimensional configuration in Figure 2. Despite the observed variability of the three-dimensional surfaces, the flattened boundary shape is consistent, as indicated by the qualitative similarity of the best fitting ellipse to the boundary of V1 for each sample. The qualitative variability of V1 with respect to the pattern of mean curvature of the cortex is evident from inspection of Figure 2. In addition, the location of the occipital pole varies considerably with respect to the location of V1, consistent with the observations of Horton and Hedley-Whyte (1984). Note that the average RMS error of the ellipse fit to the V1 boundary over all samples is only 1.65 mm, or roughly 2% of the average length of the major axis of V1 (about 80 mm). This indicates that the ellipse is effective as a simple approximation to the boundary shape of V1.

Statistical shape analysis

The intrinsic shape of the boundary of V1 across all subjects exhibits low variance. Table 2 shows the shape parameters, and their standard deviation, for each hemisphere. The mean aspect ratio is 1.85, which is consistent with previous qualitative reports of the aspect ratio of macaque V1 (Van Essen et al., 1984; LeVay et al., 1985; Duffy et al., 1998). Note that the magnitude of the semi-major and semi-minor axes of the best fitting ellipse varies across subjects, with a ratio of the standard deviation to the mean (the coefficient of variation) of 15% and 12%, respectively. In contrast, the aspect ratio of the ellipse shows only a 6.5% coefficient of variation. The surface area of V1 exhibits a 26% coefficient of variation, but when surface area is normalized, the coefficient of variation drops to 3.8% for the major axis and 2.8% for the minor axis. Comparison of these statistics highlights the regularity of the intrinsic shape of V1 relative to its absolute size and extrinsic geometry. In addition, no significant difference between left and right V1 was found using a one-way ANOVA comparing the means of the aspect ratios ($p = 0.23$) or the surface areas ($p = 0.83$).

Spatial distribution of shape similarity

The shape similarity of V1 was evaluated by testing the probability of overlap of flattened V1 across samples after alignment via rigid-body isometric transformations found by ICP. Figure 3(A) shows regions of constant probability of falling inside V1 for each location as the same color. The spatial profile of error in the probability map shows a tightly clustered distribution that is similar at all points around the boundary of V1. This would not be the case if the shape of V1 exhibited high variance.

Figure 3(B) shows the percent overlap of V1 averaged over all combinations of groups of between two to

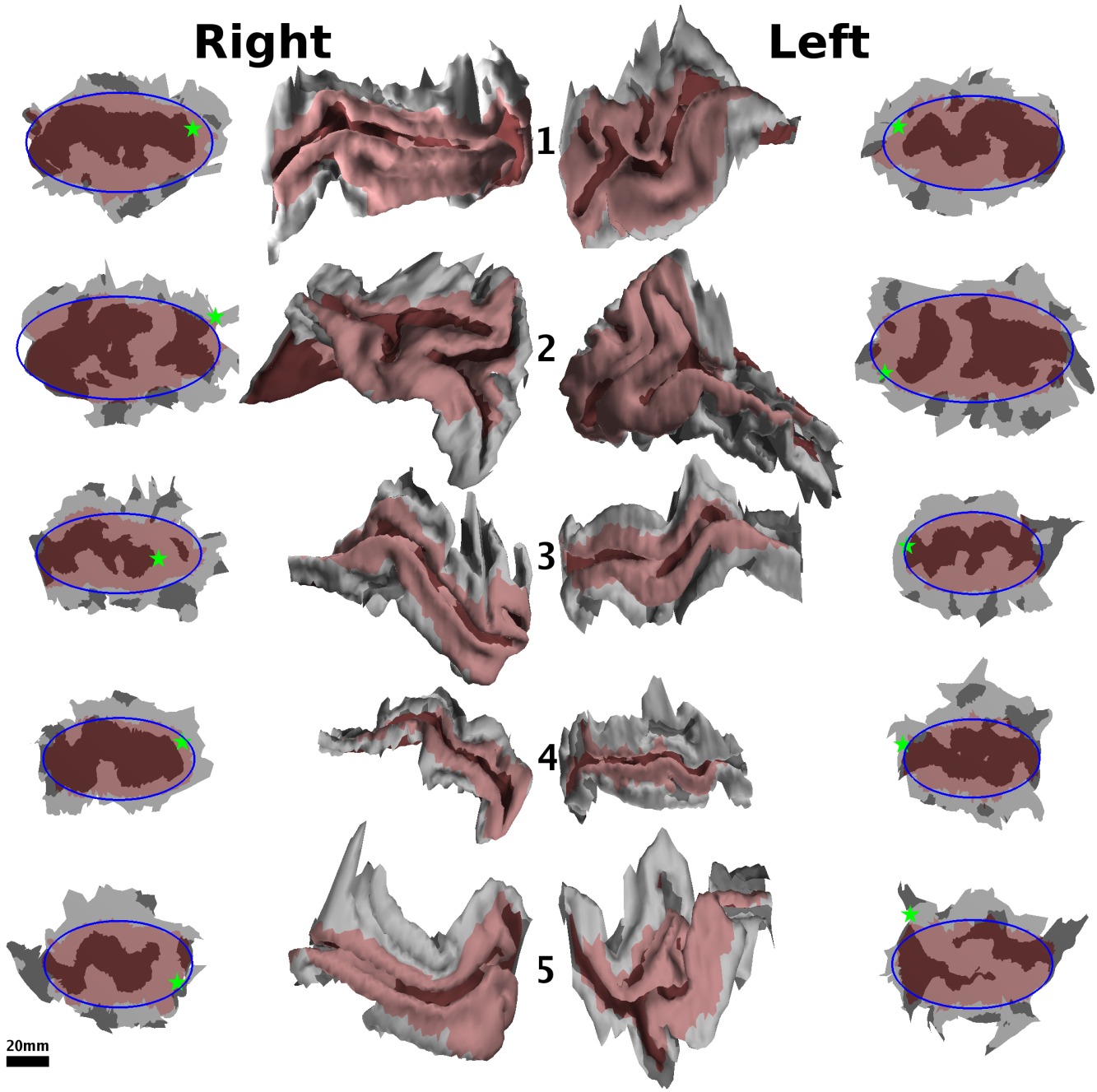

Figure 2: The surfaces reconstructed from MRI data of all samples. The surface of the stria of Gennari is shown in red. The sign of the mean curvature of the cortical surface is indicated by light and dark shading. V1 of the five right hemispheres are shown in the second column with posterior to the right and dorsal to the top. The five left hemispheres are shown in the third column with posterior to the left and dorsal to the top. Overall the shape, location, and size of V1 shows substantial variation. The first and fourth columns show flattened two-dimensional configurations of the V1 surfaces shown in the second and third columns, respectively. The boundary of flattened V1 exhibits a consistent shape, whereas the three-dimensional shape exhibits more variability. The best fitting ellipse to the boundary of V1 is superimposed in blue. The location of the occipital pole is indicated by a green star. The scale bar applies to the flattened surfaces only, as the three-dimensional surfaces have been enlarged to show detail but are to scale with one another.

Table 2: The relative RMS flattening error, surface statistics, RMS error in the ellipse fit, and shape parameters for each of the ten hemispheres reconstructed.

hemisphere	**flattening error**	**flattening time** (min)	**area** (mm^2)	**perimeter** (mm)	e_1 (mm)	e_2 (mm)	**ellipse fit error** (mm)	**aspect ratio**
LH1	6.8%	18	3290	331	42.2	22.2	1.76	1.90
RH1	5.8%	20	3640	318	44.0	23.5	1.69	1.87
LH2	5.2%	73	4230	359	48.0	25.6	1.58	1.87
RH2	5.2%	23	3930	311	48.1	24.4	1.88	1.98
LH3	5.3%	11	2210	247	32.4	19.3	1.19	1.68
RH3	4.8%	19	2500	276	38.8	18.8	2.05	2.07
LH4	6.3%	8	2040	293	31.9	18.4	1.57	1.73
RH4	5.6%	5	2380	278	35.6	19.3	1.33	1.85
LH5	5.9%	10	2770	308	37.8	20.8	1.88	1.82
RH5	7.2%	10	2650	294	34.8	20.3	1.62	1.71
mean ± std.	5.8% ± 0.7%	20 ± 20	2960 ± 760	302 ± 31	39.4 ± 6.0	21.2 ± 2.5	1.65 ± 0.26	1.85 ± 0.12

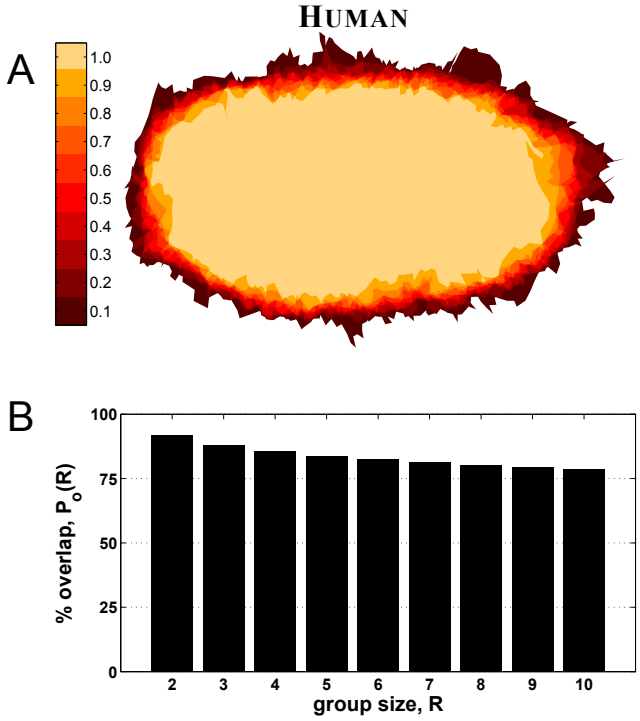

Figure 3: (A) The probability map of each location in the co-registered hemispheres falling inside V1, with the color of the pixel representing the probability, as indicated by the colorbar to the left. (B) The average percent overlap of V1 for different group sizes.

ten hemispheres. The overlap of all ten surfaces, $P_o(10)$ (defined in Eq.(1)), is 78.8%, indicating low variance in individual surface shape compared to the average shape. The percent blurring, P_b (defined in Eq.(2)), over all subjects was 25.0% under shape-preserving registration, indicating that the spread of individual surface shape is low across the population.

In addition to examining the distribution of shape similarity, the spatial distribution of geometric distortion introduced by the near-isometric flattening was computed after alignment. Both the average distance distortion and the average area distortion were mapped in the aligned space, and were found to be relatively low and uniform across V1. The average distance distortion in V1 was 5.6% with a 0.4% standard deviation, and the average area distortion was 11.5% with a 3.3% standard deviation. The spatial distribution across subjects of the mean and Gaussian curvature was also computed, showing a consistent relationship between the curvature pattern of the calcarine sulcus and the border of V1. More detail about both the average flattening distortion and the average curvature is presented in the Supplementary Material.

Effect of neurological disease

Cortical thickness has been shown to decrease due to both AD (Frisoni, 1996; De Leon et al., 1997; Jack et al., 1997) and HD (Vonsattel and DiFiglia, 1998; Halliday et al., 1998; Rosas et al., 2005), but neither disease has been shown to effect the boundaries of cortical areas. To verify that neurological disease did not influence the shape of V1, the statistics of the aspect ratio were computed while leaving out the three samples from diseased individuals. The mean aspect ratio was unchanged, and the standard deviation dropped by only about 10%, indicating that disease had little, if any, effect on the shape. Also, a one-way, unbalanced ANOVA was conducted to test if the mean V1 aspect ratio was different between the group of neurologically normal and group of diseased brains. The null hypothesis that the means of these two groups were equal could not be rejected ($p = 0.89$).

Boundary shape of macaque V1

Since macaques are often assumed to provide a human surrogate in invasive visual experiments, we investigated the intrinsic shape of macaque V1 for comparison with the human V1 shape. To establish the shape of V1 in macaque, the boundary of each of the eight hand-flattened V1 samples published by Horton and Hocking (1996) was identified, and the boundaries were co-registered in the same way as the computationally flattened human V1 surfaces. The mean and standard deviation of the aspect ratio of macaque V1 is 2.0 ± 0.08, very similar to the aspect ratio of human V1. Despite this apparent shape similarity, an unbalanced, one-way ANOVA shows that the null hypothesis that the means of the aspect ratios between the species are the same is rejected ($p = 0.006$). Nevertheless, the difference in the means is less than 8%, which is small given the substantial differences in the extrinsic geometry between human and macaque.

The overlap for each pixel was computed just as it was for the human data, and the resulting probability map is shown in Figure 4(A). A bar plot showing the average percent overlap $P_o(R)$ for different group sizes is shown in Figure 4(B). The percent blurring P_b for the macaque V1 samples shown here is 10.0%. Overall, the variability in the boundary shape of macaque V1 is low, and its shape is quite similar to that of human V1.

Discussion

Intersubject registration

Previous studies reporting intersubject variability in V1 have relied on intersubject registration methods to align V1. Because these methods use cortical geometric features indirectly related to the location of V1 for alignment, previous reports confound variability in cortical geometry with V1 variability. However, regularity of the intrinsic shape of V1 allows a new interpretation of previous work for comparison of intersubject registration methods. Intersubject registration is commonly used in multi-subject functional imaging experiments. Therefore, determining the most effective method is important for maximizing the benefit of intersubject averaging.

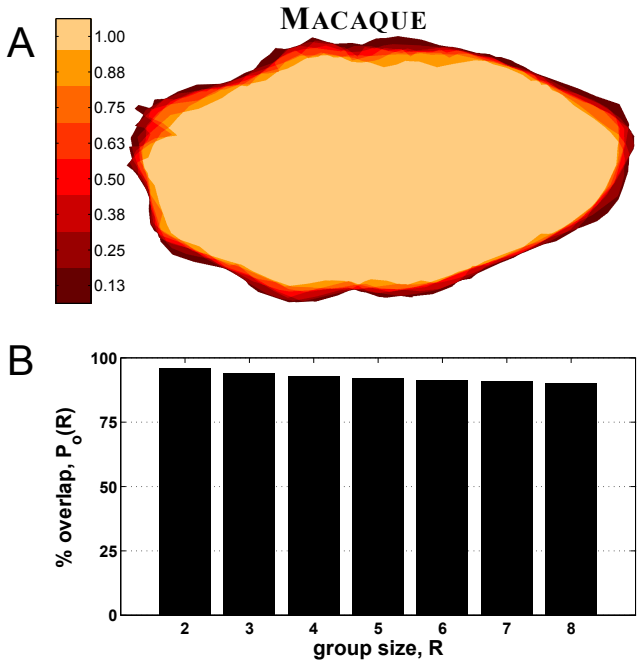

Figure 4: (A) Probability map of the eight hand-flattened macaque V1 surfaces published by Horton and Hocking (1996). (B) The average percent overlap of the flattened macaque V1 for various group sizes.

Volume-based registration

Volume-based techniques for registration attempt to align the cortical geometry of a group of subjects with respect to a reference three-dimensional stereotaxic coordinate system. Linear volume-based registration (Talairach and Tournoux, 1988) uses linear transformations to warp brain images into the reference space. Amunts et al. (2000) used a linear volume-based registration technique to register cytoarchitectonically identified V1 in ten brains, observing overlap of V1 for all subjects of 30 mm^3, or 0.13%, indicating virtually no overlap.

Overlap using linear volume-based registration has been evaluated in comparison to surface-based methods for functionally defined V1 by Fischl et al. (1999), who used standard fMRI-based visuotopic mapping techniques (Sereno et al., 1995) to determine the functionally-defined border of V1 in 11 human subjects, then used linear volume-based registration to co-register the brains of the subjects. The percent blurring for V1 using volume-based registration was about 600%. Intuitively, this amount of blurring means that it is possible for the V1 of five subjects to be totally disjoint after linear volume-based registration, suggesting that it performs poorly at corresponding functional areas across subjects.

Nonlinear volume-based registration methods such as the spatial normalization performed by the Statistical Parametric Mapping (SPM) Toolbox (Friston et al., 1995), as well as the methods described by Roland et al. (1994) and Schormann and Zilles (1998), perform a voxel-wise nonlinear warping of one brain into a reference brain by determining the deformation field that results in the best match between the voxel intensities of the respective structural volumes. Although the goal of nonlinear volume-based registration is to produce overlap between corresponding features across subjects by changing cortical geometry to best fit into a reference brain, several studies have shown that the resulting overlap of cortical features across subjects is quite low (Roland et al., 1997; Crum et al., 2003). Most notably, Nieto-Castanon et al. (2003) parcellated cortex via hand tracing in nine subjects, then applied SPM nonlinear volume-based registration, observing almost no overlap.

The high percent overlap and low percent blurring under the intrinsic shape-based registration technique used in this study indicates that volume-based intersubject registration methods fail to capture the regularity that does exist in the shape of human V1. This is due in part to the inability of volume-based methods to represent the intrinsic geometry of the cortical surface.

Surface-based registration

Surface-based registration methods (Drury et al., 1996; Sereno et al., 1996; Thompson and Toga, 1996; Davatzikos, 1997; Fischl et al., 1999) use an explicit representation of the cortical sheet and a coordinate system defined on it to accomplish intersubject registration. Accurate surface-based methods preserve the natural structure of the cortex, and therefore have the potential to provide greater overlap of functional areas when intersubject comparison is performed.

Fischl et al. (1999) presented a surface-based registration technique, called Automated Spherical Warping, where a triangular mesh representation of the cortical surface segmented from an MRI volume is registered to a sphere while preserving geometry, then the spherical coordinate system for one subject is nonlinearly warped into a reference coordinate system via correspondence of the primary folds of the subject and reference brains. Primary folds develop early in the cortical folding process, and exhibit the least intersubject variability (Connolly, 1950; Bailey and von Bonin, 1951; Chi et al., 1977). To discount the more variable secondary and tertiary folds, Fischl et al. (1999) registered using a measure of sulcal depth called "average convexity", which they relate to the primary folding pattern.

To demonstrate the ability of surface-based registration to align cortical areas across subjects, Fischl et al. (1999) tested the resulting overlap in V1 delineated independently using functional data. Automated Spherical Warping results in a percent blurring for V1 of about 80%, which is a sevenfold improvement over linear volume-based registration. Because of the regularity in the intrinsic shape of human V1, surface-based registration methods are more successful at producing overlap of V1 than volume-based registration methods. This is a direct consequence of the ability of surface-based registration to represent the intrinsic geometry of the cortical sheet.

Measuring variability

Several previous studies have addressed the intrinsic shape of V1 in species other than human (Van Essen et al., 1984; Tootell et al., 1988; Duffy et al., 1998; Bush and Allman, 2004), but to date there has been no quantitative study of the intrinsic, two-dimensional shape in human. In addition, previous studies have reported considerable variability in the extrinsic geometry of human V1 (Stensaas et al., 1974; Rademacher et al., 1993; Roland et al., 1997; Amunts et al., 2000), as well as other cortical areas (Zilles et al., 1995; Amunts et al., 1999; Geyer et al., 1999; Morosan et al., 2001; Rademacher et al., 2001; Amunts et al., 2004, 2005; Uylings et al., 2005; Eickhoff et al., 2006), but these studies did not investigate the intrinsic geometry of the cortical surface, and therefore report much larger variability in cortical geometry than the present study.

Human and macaque V1 are consistently positioned around the calcarine sulcus, but the detailed folding pattern and size vary considerably across individuals. This point is illustrated in Figure 5, which shows V1 and V2 (Brodmann areas 17 and 18) in six human hemispheres studied by Filimonov (1932), in which the extrinsic geometry of V1 appears to vary considerably across different subjects.

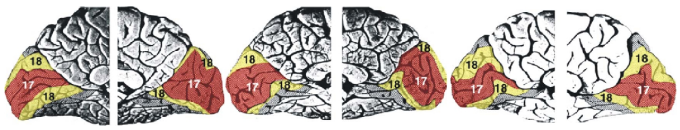

Figure 5: Medial views of six hemispheres presented by Filimonov (1932) [reproduced from Uylings et al. (2005)], in which BA 17 is labeled red, and BA 18 is labeled yellow.

As discussed above, the overlap and blurring observed in this study indicates much less variability in V1 than reported by Amunts et al. (2000) or Fischl et al. (1999). However, both of these studies sought to generate a probabilistic atlas, providing a method for estimating the location of V1 based on features other than V1, and thus their results are not directly comparable to the results of this study. Here, V1 was registered directly while preserving intrinsic geometry to determine the variability in its intrinsic shape. Because of the regularity of the intrinsic shape of V1 and the knowledge of its boundary, the average overlap of 78.8% and percent blurring of

25.0% for ten hemispheres found in this study establishes a lower bound on population variability.

Similarity of V1 shape in macaque and human

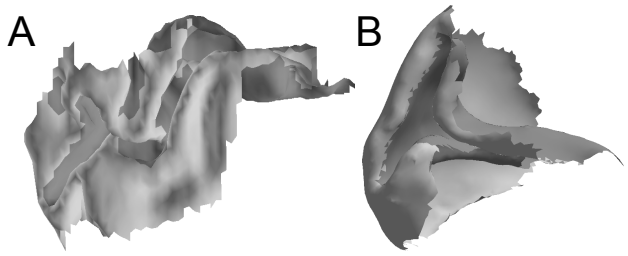

Figure 6: (A) A medial view of human V1 from hemisphere LH1. (B) A medial view of macaque V1 included in the CARET database (Van Essen et al., 2001).

The macaque visual system is commonly used as a model for the human visual system in electrophysiological, histological, and functional imaging experiments. However, the extrinsic geometry of V1 in these two species is quite different, as shown in Figure 6. Nevertheless, recently it has been shown that the topographic map in V1, which determines the V1 boundary, is similar in the two species (Polimeni et al., 2006b).

The wedge–dipole model of Balasubramanian et al. (2002) provides an accurate model of the full visuotopic map in macaque (Polimeni et al., 2006a), and has also been shown via fMRI to fit the para-foveal structure of human V1 visuotopy (Polimeni et al., 2005). Such complex logarithm or "logmap" models of two-dimensional cortical visuotopy have been shown to have properties advantageous for certain classes of computations on the visual input, and these properties have been exploited in space-variant computer vision applications such as image compression (Chaikin and Weiman, 1980; Rojer and Schwartz, 1990; Wallace et al., 1994), fast image segmentation via anisotropic diffusion (Fischl et al., 1998), navigation (Tistarelli and Sandini, 1993; Wagner et al., 2005), and image deblurring (Bonmassar and Schwartz, 1999).

The shape of V1 derived from the wedge–dipole model is roughly elliptical, but establishing a standard aspect ratio of V1 allows direct comparison of the anatomically and functionally determined standard shape of V1. Figure 7 shows the superposition of an ellipse of the mean aspect ratio determined in this study and the wedge–dipole model. V1 parameters were measured from electrophysiological experiments of full-field two-dimensional V1 topography in the macaque (Polimeni et al., 2006a) and an fMRI measurement of the para-foveal visuotopic map in human (Polimeni et al., 2005).

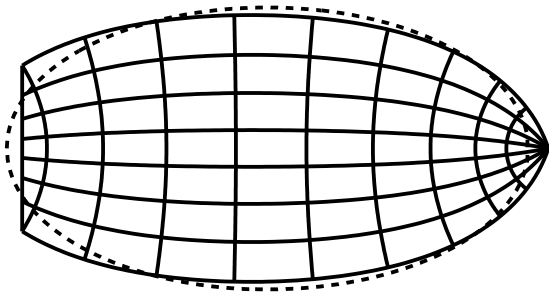

Figure 7: The mapping of the visual hemifield onto V1 predicted by the wedge–dipole model with measured parameter values [$a = 0.6$, $b = 80.0$, $\alpha = 0.8$ (Polimeni et al., 2005, 2006a)] is shown by the solid line. The ellipse with the average aspect ratio for human V1 (1.85) is shown by the dotted line. The shapes are strikingly similar.

Excellent agreement between the boundary shape determined in this study with that predicted by the wedge–dipole visuotopic model provides independent validation of the model, and also emphasizes the sim-

ilarity in the shape of human and macaque V1. In addition, this validation provides anatomical evidence for regularity of the topographic mapping itself, both across subjects and between these two species.

References

Amunts, K., Kedo, O., Kindler, M., Pieperhoff, P., Mohlberg, H., Shah, N., Habel, U., Schneider, F., Zilles, K., 2005. Cytoarchitectonic mapping of the human amygdala, hippocampal region and entorhinal cortex: intersubject variability and probability maps. Anat Embryol 210 (5), 343–352.

Amunts, K., Malikovic, A., Mohlberg, H., Schormann, T., Zilles, K., 2000. Brodmann's areas 17 and 18 brought into stereotaxic space—where and how variable? NeuroImage 11 (1), 66–84.

Amunts, K., Schleicher, A., Burgel, U., Mohlberg, H., Uylings, H. B., Zilles, K., 1999. Broca's region revisited: cytoarchitecture and intersubject variability. J Comp Neurol 412 (2), 319–341.

Amunts, K., Weiss, P., Mohlberg, H., Pieperhoff, P., Eickhoff, S., Gurd, J., Marshall, J., Shah, N., Fink, G., Zilles, K., 2004. Analysis of neural mechanisms underlying verbal fluency in cytoarchitectonically defined stereotaxic space–the roles of Brodmann areas 44 and 45. NeuroImage 22 (1), 42–56.

Augustinack, J. C., van der Kouwe, A. J., Blackwell, M. L., Salat, D. H., Wiggins, C. J., Frosch, M. P., Wiggins, G. C., Potthast, A., Wald, L. L., Fischl, B. R., 2005. Detection of entorhinal layer II using 7 Tesla magnetic resonance imaging. Ann Neurol 57 (4), 489–494.

Bailey, P., von Bonin, G., 1951. The Isocortex of Man. University of Illinois, Urbana, IL.

Balasubramanian, M., Polimeni, J., Schwartz, E. L., 2002. The V1–V2–V3 complex: quasiconformal dipole maps in primate striate and extra-striate cortex. Neural Netw 15 (10), 1157–1163.

Balasubramanian, M., Polimeni, J. R., Schwartz, E. L., 2005. Quasi-isometric flattening of large-scale cortical surfaces [Abstract]. Soc Neurosci Abstr.

Balasubramanian, M., Polimeni, J. R., Schwartz, E. L., 2006. Quantitative evaluation and comparison of cortical flattening algorithms [Abstract]. Soc Neurosci Abstr.

Barbier, E. L., Marrett, S., Danek, A., Vortmeyer, A., van Gelderen, P., Duyn, J., Bandettini, P., Grafman, J., Koretsky, A. P., 2002. Imaging cortical anatomy by high-resolution MR at 3.0T: detection of the stripe of Gennari in visual area 17. Magn Reson Med 48 (4), 735–738.

Besl, P. J., McKay, N. D., 1992. A method for registration of 3-dimensional shapes. IEEE Trans Pat Anal and Mach Intel 14 (2), 239–256.

Boissonnat, J.-D., 1988. Shape reconstruction from planar cross sections. Comput Vis Graph Image Process 44 (1), 1–29.

Bolton, J. S., 1900. The exact histological localisation of the visual area of the human cerebral cortex. Philos Trans R Soc Lond B Biol Sci 193, 165–222.

Bonmassar, G., Schwartz, E. L., 1999. Real-time restoration of images degraded by uniform motion blur in foveal active vision systems. IEEE Trans Image Proc 8, 1838–1842.

Boyd, J. D., Matsubara, J. A., 2005. Repositioning the stria of Gennari [Abstract]. Soc Neurosci Abstr.

Bridge, H., Clare, S., Jenkinson, M., Jezzard, P., Parker, A. J., Matthews, P. M., 2005. Independent anatomical and functional measures of the V1/V2 boundary in human visual cortex. J Vis 5 (2), 93–102.

Brodmann, K., 1918. Individuelle variationen der sehsphare und ihre bedeutung fur die klink der hinterphauptschusse. Allgz Psychiat (Berline) 74, 564–568.

Bush, E. C., Allman, J. M., 2004. Three-dimensional structure and evolution of primate primary visual cortex. Anat Rec A Discov Mol Cell Evol Biol 281 (1), 1088–1094.

Chaikin, G. M., Weiman, C. F. R., 1980. Conformal computational geometry for machine vision. Proc. 5th International Conference on Pat Recog Image Proc, 1106–1110.

Chi, J. G., Dooling, E. C., Gilles, F. H., 1977. Gyral development of the human brain. Ann Neurol 1 (1), 86–93.

Clark, V. P., Courchesne, E., Grafe, M., 1992. In vivo myeloarchitectonic analysis of human striate and extrastriate cortex using magnetic resonance imaging. Cereb Cortex 2 (5), 417–424.

Clark, W., 1941. The laminar organization and cell content of the lateral geniculate body in the monkey. J Anat 75, 225.

Connolly, C., 1950. External morphology of the primate brain. Thomas.

Crum, W. R., Griffin, L. D., Hill, D. L. G., Hawkes, D. J., 2003. Zen and the art of medical image registration: correspondence, homology, and quality. NeuroImage 20 (3), 1425–1437.

Davatzikos, C., 1997. Spatial transformation and registration of brain images using elastically deformable models. Comput Vis Image Underst 66 (2), 207–222.

De Leon, M. J., George, A. E., Golomb, J., Tarshish, C., Convit, A., Kluger, A., De Santi, S., McRae, T., Ferris, S. H., Reisberg, B., Ince, C., Rusinek, H., Bobinski, M., Quinn, B., Miller, D. C., Wisniewski, H. M., 1997. Frequency of hippocampal formation atrophy in normal aging and Alzheimer's disease. Neurobiol Aging 18 (1), 1–11.

Do Carmo, M. P., 1976. Differential Geometry of Curves and Surfaces. Prentice-Hall, New Jersey.

Drury, H. A., Van Essen, D. C., Joshi, S. C., Miller, M. I., 1996. Analysis and comparison of areal partitioning schemes using two-dimensional fluid deformations [Abstract]. NeuroImage (S130).

Duffy, K. R., Murphy, K. M., Jones, D. G., 1998. Analysis of the postnatal growth of visual cortex. Vis Neurosci 15 (5), 831–839.

Eickhoff, S. B., Schleicher, A., Zilles, K., Amunts, K., 2006. The human parietal operculum. I. Cytoarchitectonic mapping of subdivisions. Cereb Cortex 16 (2), 254–267.

Fatterpekar, G. M., Naidich, T. P., Delman, B. N., Aguinaldo, J. G., Gultekin, S. H., Sherwood, C. C., Hof, P. R., Drayer, B. P., Fayad, Z. A., 2002. Cytoarchitecture of the human cerebral cortex: MR microscopy of excised specimens at 9.4 Tesla. AJNR Am J Neuroradiol 23 (8), 1313–1321.

Filimonov, I. N., 1932. Uber die variabilitat der grosshirn rindenstruktur mitt 2: Regio occipitalis beim erwachsenen menschen. J Psychol Neurol 44, 1–96.

Fischl, B., Cohen, M., Schwartz, E. L., 1998. Rapid anisotropic diffusion using space-variant vision. Int J Computer Vis 28 (3), 199–213.

Fischl, B., Salat, D. H., van der Kouwe, A. J., Makris, N., Segonne, F., Quinn, B. T., Dale, A. M., 2004. Sequence-independent segmentation of magnetic resonance images. NeuroImage 23 (Suppl 1), S69–S84.

Fischl, B., Sereno, M. I., Tootell, R. B., Dale, A. M., 1999. High-resolution intersubject averaging and a coordinate system for the cortical surface. Hum Brain Mapp 8 (4), 272–284.

Frisoni, G. B., 1996. Linear measures of atrophy in mild alzheimer disease. Amer J Neurorad 17 (5), 913–923.

Friston, K. J., Ashburner, J., Frith, C. D., Poline, J., Heather, J. D., Frackowiak, R. S. J., 1995. Spatial registration and normalization of images. Hum Brain Mapp 3 (3), 165–189.

Geyer, S., Schleicher, A., Zilles, K., 1999. Areas 3a, 3b, and 1 of human primary somatosensory cortex. NeuroImage 10 (1), 63–83.

Griffin, L. D., 1994. The intrinsic geometry of the cerebral cortex. J Theor Biol 166 (3), 261–273.

Halliday, G. M., McRitchie, D. A., Macdonald, V., Double, K. L., Trent, R. J., McCusker, E., 1998. Regional specificity of brain atrophy in Huntington's disease. Exp Neurol 154 (2), 663–672.

Henschen, S., 1890. Klinische und anatomische Beiträge zur Pathologie des Gehirns. Almquist and Wiksell.

Hinds, O. P., Polimeni, J. R., Blackwell, M. L., Wiggins, C. J., Wiggins, G., van der Kouwe, A. J., Wald, L. L., Schwartz, E. L., Fischl, B., 2005a. Surface reconstruction of *ex-vivo* human V1 through identification of the stria of Gennari using MRI at 7 T [Abstract]. Hum Brain Mapp Annual Meeting (140).

Hinds, O. P., Polimeni, J. R., Blackwell, M. L., Wiggins, C. J., Wiggins, G. C., van der Kouwe, A., Wald, L. L., Schwartz, E. L., Fischl, B., 2005b. Reconstruction and analysis of human V1 by imaging the stria of Gennari using MRI at 7 T [Abstract]. Soc Neurosci Abstr.

Hinds, O. P., Polimeni, J. R., Schwartz, E. L., 2006. Brain surface reconstruction from slice contours [Abstract]. NeuroImage 31 (1), S445.

Horton, J. C., Hedley-Whyte, E. T., 1984. Mapping of cytochrome oxidase patches and ocular dominance columns in human visual cortex. Philos Trans R Soc Lond B Biol Sci 304 (1119), 255–272.

Horton, J. C., Hocking, D. R., 1996. Intrinsic variability of ocular dominance column periodicity in normal macaque monkeys. J Neurosci 16 (22), 7228–7239.

Jack, C. R., Petersen, R. C., Xu, Y. C., Waring, S. C., O'Brien, P. C., Tangalos, E. G., Smith, G. E., Ivnik, R. J., Kokmen, E., 1997. Medial temporal atrophy on MRI in normal aging and very mild Alzheimer's disease. Neurology 49 (3), 786–794.

Jenkinson, M., Bannister, P., Brady, M., Smith, S., 2002. Improved optimization for the robust and accurate linear registration and motion correction of brain images. NeuroImage 17 (2), 825–841.

LeVay, S., Connolly, M., Houde, J., Van Essen, D. C., 1985. The complete pattern of ocular dominance stripes in the striate cortex and visual field of the macaque monkey. J Neurosci 5 (2), 486–501.

Lorensen, W. E., Cline, H. E., 1987. Marching cubes: A high resolution 3D surface construction algorithm. Comput Graph 21 (3), 163–169.

Meyers, D., Skinner, S., Sloan, K., 1992. Surfaces from contours. ACM Trans Graph 11 (3), 228–258.

Morosan, P., Rademacher, J., Schleicher, A., Amunts, K., Schormann, T., Zilles, K., 2001. Human primary auditory cortex: cytoarchitectonic subdivisions and mapping into a spatial reference system. NeuroImage 13 (4), 684–701.

Nieto-Castanon, A., Ghosh, S. S., Tourville, J. A., Guenther, F. H., 2003. Region of interest based analysis of functional imaging data. NeuroImage 19 (4), 1303–1316.

Pfefferbaum, A., Sullivan, E. V., Adalsteinsson, E., Garrick, T., Harper, C., 2004. Postmortem MR imaging of formalin-fixed human brain. NeuroImage 21 (4), 1585–1595.

Polimeni, J. R., Balasubramanian, M., Schwartz, E. L., 2006a. Multi-area visuotopic map complexes in macaque striate and extra-striate cortex. Vision Res 46 (20), 3336–3359.

Polimeni, J. R., Hinds, O. P., Balasubramanian, M., Fischl, B., Schwartz, E. L., 2006b. Characterization of cortical visuotopy in human and macaque: quantitative similarities across subjects and species [Abstract]. NeuroImage 31 (1), S198.

Polimeni, J. R., Hinds, O. P., Balasubramanian, M., van der Kouwe, A., Wald, L. L., Dale, A. M., Fischl, B., Schwartz, E. L., 2005. The human V1–V2–V3 visuotopic map complex measured via fMRI at 3 and 7 Tesla [Abstract]. Soc Neurosci Abstr.

Polyak, S., 1933. A contribution to the cerebral representation of the retina. J Comp Neurol 57 (3), 541–617.

Polyak, S., 1957. The Vertebrate Visual System. University of Chicago Press, Chicago.

Popoff, N., 1927. Zur kenntnis der grosse der area striata und die methodik ihrer ausmessung. J Psychol Neurol 34, 238–242.

Putnam, T. J., 1926. Studies on the central visual system. IV: The details of the organization of the geniculostriate system in man. Arch Neurol Psychiatry 16, 683–707.

Rademacher, J., Caviness, V. S., Steinmetz, H., Galaburda, A. M., 1993. Topographical variation of the human primary cortices: implications for neuroimaging, brain mapping, and neurobiology. Cereb Cortex 3 (4), 313–329.

Rademacher, J., Morosan, P., Schormann, T., Schleicher, A., Werner, C., Freund, H. J., Zilles, K., 2001. Probabilistic mapping and volume measurement of human primary auditory cortex. NeuroImage 13 (4), 669–683.

Rojer, A. S., Schwartz, E. L., 1990. Design considerations for a space-variant visual sensor with complex-logarithmic geometry. In: Proceedings of the 10th International Conference on Pattern Recognition. Vol. 2. pp. 278–285.

Roland, P. E., Geyer, S., Amunts, K., Schormann, T., Schleicher, A., Malikovic, A., Zilles, K., 1997. Cytoarchitectural maps of the human brain in standard anatomical space. Hum Brain Mapp 5 (4), 222–227.

Roland, P. E., Graufelds, C. J., Wacaronhlin, J., Ingelman, L., Andersson, M., Ledberg, A., Pedersen, J., Akerman, S., Dabringhaus, A., Zilles, K., 1994. Human brain atlas: For high-resolution functional and anatomical mapping. Hum Brain Mapp 1 (3), 173–184.

Rosas, H. D., Hevelone, N. D., Zaleta, A. K., Greve, D. N., Salat, D. H., Fischl, B., 2005. Regional cortical thinning in preclinical Huntington disease and its relationship to cognition. Neurology 65 (5), 745–747.

Schormann, T., Zilles, K., 1998. Three-dimensional linear and nonlinear transformations: an integration of light microscopical and MRI data. Hum Brain Mapp 6 (5–6), 339–347.

Sereno, M. I., Dale, A. M., Liu, A., Tootell, R. B. H., 1996. A surface-based coordinate system for a canonical cortex. [Abstract]. NeuroImage (S252).

Sereno, M. I., Dale, A. M., Reppas, J. B., Kwong, K. K., Belliveau, J. W., Brady, T. J., Rosen, B. R., Tootell, R. B., 1995. Borders of multiple visual areas in humans revealed by functional magnetic resonance imaging. Science 268 (5212), 889–893.

Stensaas, S. S., Eddington, D. K., Dobelle, W. H., 1974. The topography and variability of the primary visual cortex in man. J Neurosurg 40 (6), 747–755.

Talairach, J., Tournoux, P., 1988. Co-planar Stereotaxic Atlas of the Human Brain. Thieme, New York.

Thompson, P., Toga, A. W., 1996. A surface-based technique for warping three-dimensional images of the brain. IEEE Trans Med Imaging 15 (4), 402–417.

Tistarelli, M., Sandini, G., 1993. On the advantages of polar and log-polar mapping for direct estimation of time-to-impact from optical flow. IEEE Trans Pat Anal and Mach Intel 15 (4), 401–410.

Tootell, R. B., Switkes, E., Silverman, M. S., Hamilton, S. L., 1988. Functional anatomy of macaque striate cortex. II. Retinotopic organization. J Neurosci 8 (5), 1531–1568.

Tovi, M., Ericsson, A., 1992. Measurements of T1 and T2 over time in formalin-fixed human whole-brain specimens. Acta Radiol 33 (5), 400–404.

Uylings, H. B., Rajkowska, G., Sanz-Arigita, E., Amunts, K., Zilles, K., 2005. Consequences of large interindividual variability for human brain atlases: converging macroscopical imaging and microscopical neuroanatomy. Anat Embryol 210(5–6), 423–431.

Van Essen, D. C., Dickson, J., Harwell, J., Hanlon, D., Anderson, C. H., Drury, H. A., 2001. An integrated software system for surface-based analyses of cerebral cortex. J Am Med Inform Assoc 41, 1359–1378.

Van Essen, D. C., Newsome, W. T., Maunsell, J. H., 1984. The visual field representation in striate cortex of the macaque monkey: asymmetries, anisotropies, and individual variability. Vision Res 24 (5), 429–448.

von Economo, C., Koskinas, G. N., 1925. Die Cytoarchitektonik der Hirnrinde des erwachsenen Menschen. Springer, Berlin, abridged English translation by: Parker, S. 1929. The Cytoarchitectonics of the Human Cerebral Cortex. Humphrey Milford/Oxford University Press, London.

Vonsattel, J. P., DiFiglia, M., 1998. Huntington disease. J Neuropathol Exp Neurol 57 (5), 369–384.

Wagner, R. E., Polimeni, J. R., Schwartz, E. L., 2005. Gibson, meet topography: the dipole structure of the visual field is crucial to a robust estimate of navigation by optical flow [Abstract]. J Vis 5 (8), 895a.

Wald, L. L., Wiggins, G. C., Potthast, A., Wiggins, C. J., Triantafyllou, C., 2005. Design considerations and coil comparisons for 7 T brain imaging. Appl Magn Reson 29 (1), 19–37.

Wallace, R., Ong, P.-W., Bederson, B., Schwartz, E., 1994. Space variant image processing. Int J Compu Vis 13 (1), 71–90.

Walters, N. B., Egan, G. F., Kril, J. J., Kean, M., Waley, P., Jenkinson, M., Watson, J. D., 2003. In vivo identification of human cortical areas using high-resolution MRI: an approach to cerebral structure-function correlation. Proc Natl Acad Sci U S A 100 (5), 2981–2986.

Zilles, K., Schlaug, G., Matelli, M., Luppino, G., Schleicher, A., Qu, M., Dabringhaus, A., Seitz, R., Roland, P., 1995. Mapping of human and macaque sensorimotor areas by integrating architectonic, transmitter receptor, MRI and PET data. J Anat 187, 515–537.

Supplementary Material

MRI distortions

Susceptibility distortion

The use of a low-bandwidth FLASH pulse sequence for imaging amplifies pixel shift distortions arising from inhomogeneous magnetic susceptibility across tissue, air, and formalin compared to high-bandwidth scans (Jezzard and Balaban, 1995; Fischl et al., 2004). To test the magnitude of these geometric distortions, successive scans were acquired with positive and negative read-out directions, which, for pulse sequences employing RF excitations after data from each line of *k*-space is acquired, result in pixel displacements in opposite directions which cancel on average.

The qualitative effects of susceptibility distortions are shown in Figure S1(A) as the difference between contours of the stria drawn in the same slice of two separate acquisitions with opposite read-out direction polarities. To quantitatively evaluate the magnitude of the susceptibility distortion, the distance between the two contours was calculated at each vertex of the positive read-out contour. Figure S1(B) shows a close-up view of the outlined region of Figure S1(A). The mean distance from a vertex on the positive read-out contour to the nearest point on the negative read-out contour is 0.36 ± 0.22 mm. Since pixel shifts are in the opposite direction for the two contours, the distance between the veridical contour and a shifted one is half the distance between two oppositely shifted contours. Therefore, the average pixel shift in the region of the stria of Gennari due to susceptibility inhomogeneity is about 0.18 mm, or one voxel. It is important to note that this method underestimates the actual distortion, since calculation of the distance between contours via the closest point assumes that pixel shifts are always normal to the contours. This is not the case in general, as discussed below.

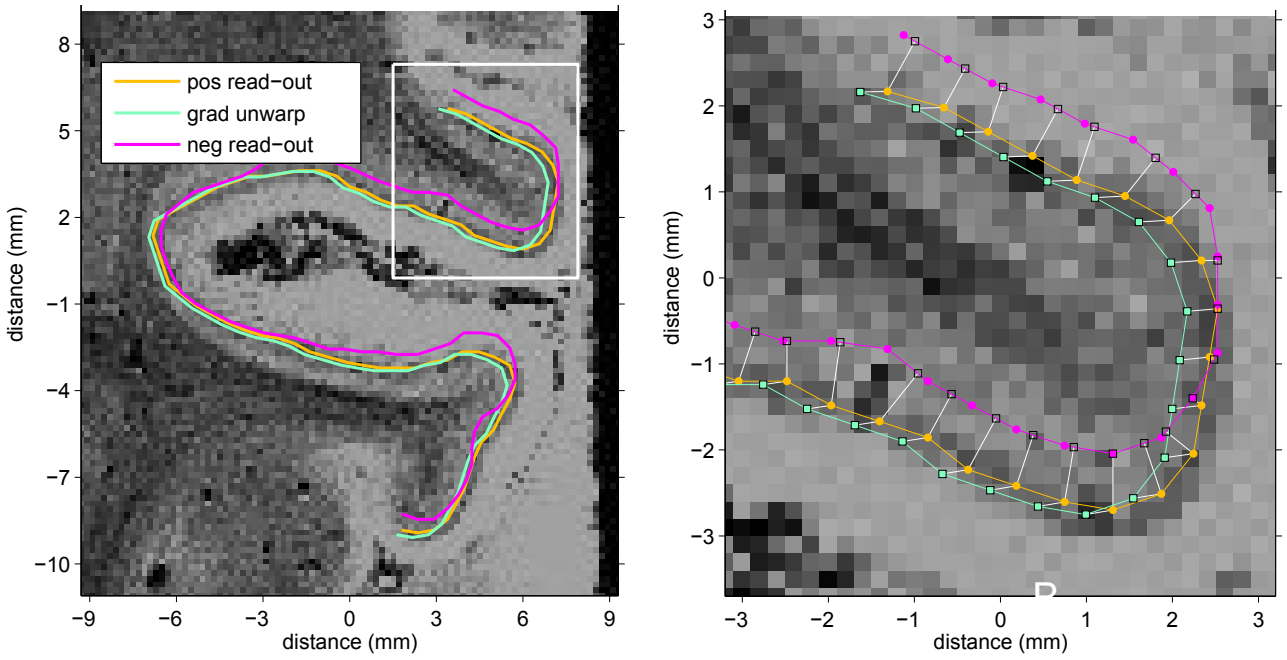

Gradient nonlinearity distortion

Another MRI distortion that affects the measured geometry of the V1 surface is geometric distortion due to the deviations from linearity of the magnetic field gradient produced by the gradient coil system. To investigate the magnitude of this type of distortion, gradient nonlinearity correction (Jovicich et al., 2006) using the three-dimensional gradient field spatial distribution specific to the coil (as supplied by the manufacturer) was applied to the same volume used to investigate susceptibility inhomogeneity distortion. The result of the gradient nonlinearity unwarping process is a vector field of displacements representing the artifactual pixel shifts due to gradient nonlinearity distortion. The coordinates of each vertex on the positive read-out contour were displaced using the gradient unwarping vector field, resulting in the unwarped contour shown in Figure S1(A).

The mean displacement of the vertices in the positive read-out contour after unwarping is 0.26 ± 0.06 mm, or about 1.5 voxels. This is 50% greater than the susceptibility inhomogeneity distortion. The effect of susceptibility inhomogeneity distortion in Figure S1(A) appears by eye to be greater than gradient nonlinearity since the negative read-out contour actually represents twice the distance shift of the actual distortion, and since the method used to calculate the displacement underestimates the distance between the positive read-out and negative read-out contours. This is a result of the different methods for computing the distance between contours for the two types of distortion. In computing gradient nonlinearity distortion magnitude, the distance between corresponding vertices on the two contours can be compared directly, since the gradient unwarping provides vertex correspondence. However, a vertex in the negative read-out contour has no corresponding vertex in the positive read-out contour, so the shortest distance between the two contours is used. This method underestimates the actual distance between contours.

Distortion correction requires warping and resampling of the original MRI data. The interpolation involved in this process smooths the data, which is undesirable when working with high-resolution images. Since we determined the effects of the MRI distortions to be smaller than the features of interest in these scans, we did not apply corrections to the data presented.

Surface area estimation

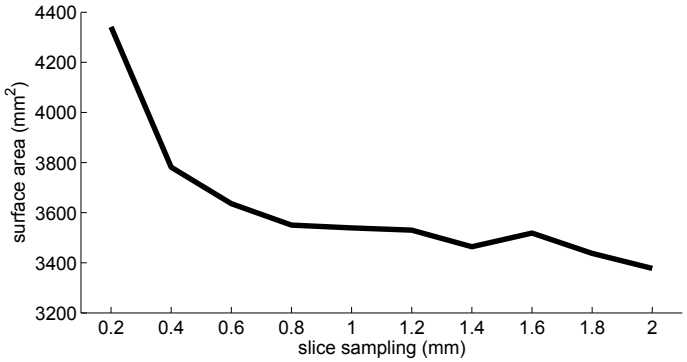

When the interslice distance was small, the human tracing error present in each slice caused numerous small-scale geometric errors in the surface mesh that appear as corrugations. These errors can lead to an overestimate of the surface-based distance between vertices on different slices. In addition, we found that a there was a substantial overestimate of the surface area of V1 when the slice distance used for reconstruction was too small, as shown in Figure S2. Although the error in slice coordinates due to contour tracing has zero mean, the distance and surface area error is strictly positive if the topology of the surface is accurate, so these small-scale geometric errors increase the observed distances and surface area. As the slice distance rises from 0.2 mm, the surface area estimate quickly asymptotes, but then starts to decrease as errors are introduced by insufficient sampling. By inspecting the agreement between the reconstructed surface mesh and the stria in the sagittal and horizontal planes, an interslice distance of 0.8 mm was determined to be appropriate for accurate surface reconstruction.

Average flattening distortion and surface curvature

To examine the spatial characteristics of distortions introduced by near-isometric flattening, the average flattening error was computed in the registered space. After registration, the per-vertex distance distortion for each entire flattened surface was binned, then the individual distance distortion maps were pooled and normalized. Any bins for which all flattened surfaces were not represented were excluded to avoid biasing the average error maps toward individual surfaces near the border of the map. The boundary of V1 on the flattened surfaces was ignored during computation of average error maps. The resulting spatial profile of average distance distortion resulting from the flattening process for all V1 surfaces after registration is shown in Figure S3(A). The average distance distortion in V1 was 5.6% with a 0.4% standard deviation. The relatively

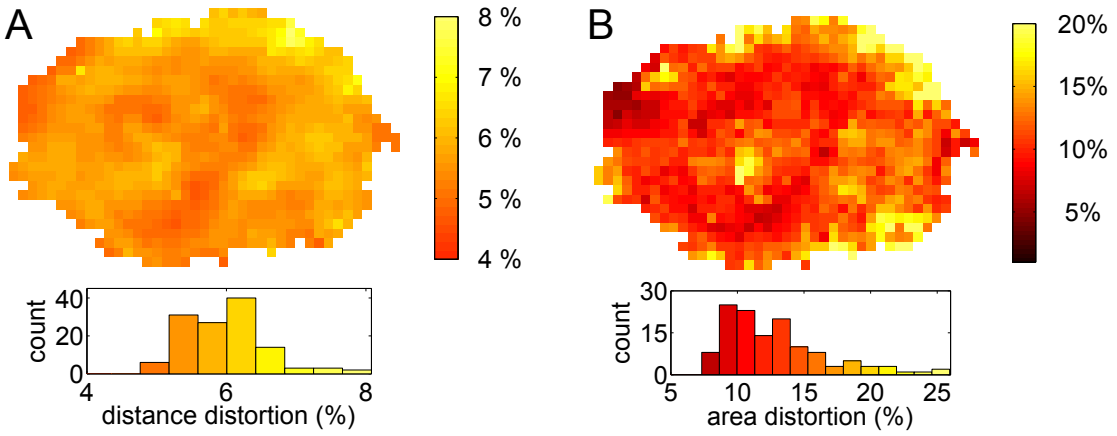

uniform profile of the distance distortion confirms that, in addition to the low average distance distortion for individual surfaces, the distance distortion across samples is spatially uncorrelated.

Figure S3(B) shows the spatial profile of the average area distortion in flattening, computed in the same way as the distance distortion map. The area distortion is higher than the distance distortion since distance distortion is explicitly minimized during the flattening process. In addition, the area error exhibits more spatial correlation than the distance distortion does. The average area distortion was 11.5% with a 3.3% standard deviation.

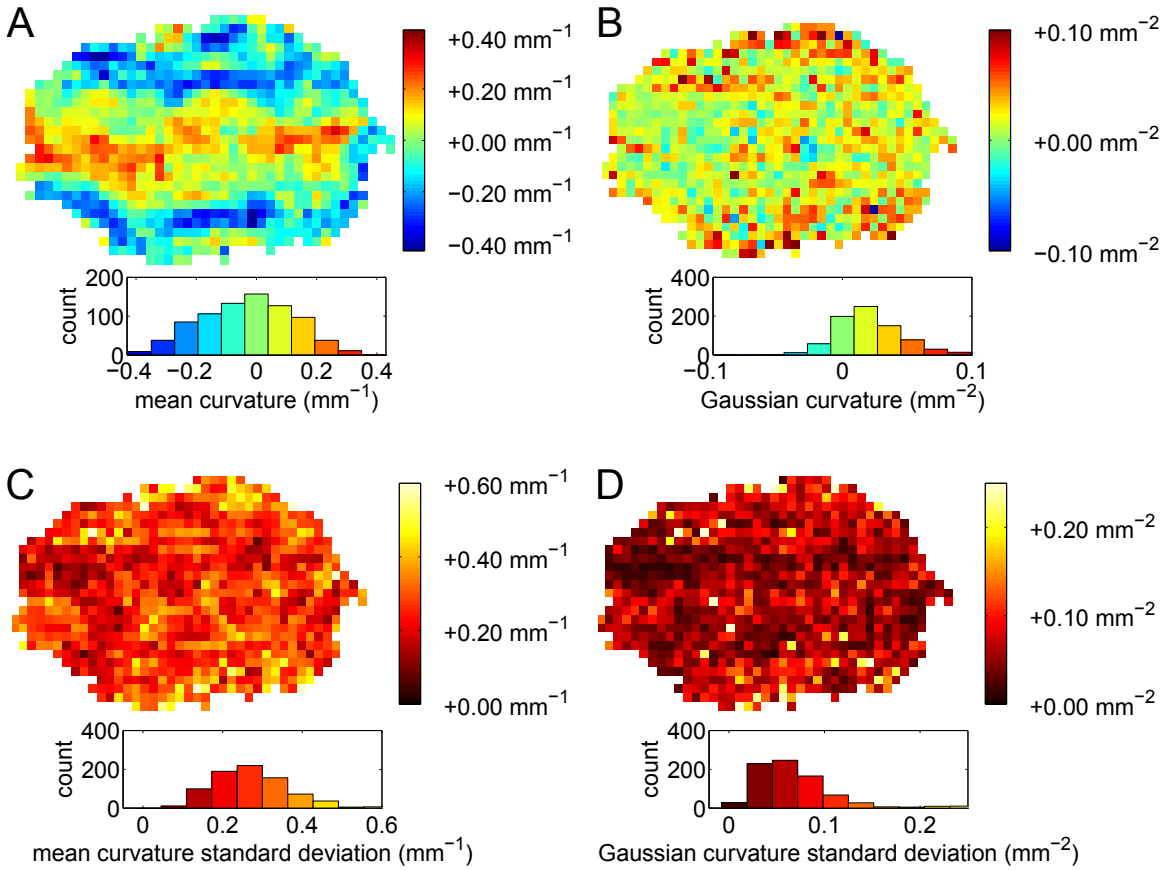

To examine regularity in the curvature pattern of the cortical sheet within V1, the mean and Gaussian curvature profiles for each sample were compared. Curvature was computed by fitting a quadratic patch to each vertex and its two-ring, then computing the mean and Gaussian curvature of the surface at the vertex via

the coefficients of the quadratic patch (Do Carmo, 1976). The average spatial maps in the registered space were computed in the same way as the flattening error maps, as described above.

The average mean curvature map after registration is shown in Figure S4(A). The strip of positive mean curvature parallel to the long axis of V1 shows the relative consistency of the fundus of the calcarine sulcus in relation to V1. The average Gaussian curvature map after registration, shown in Figure S4(B), exhibits a relatively uniform pattern.

The mean curvature map exhibits higher absolute values near the fundus and lips of the calcarine sulcus. However, high curvature cannot be reliably used to predict the location of the calcarine sulcus because the variance of the mean curvature map is high (0.3 ± 0.1 mm^{-1}) compared to the average curvature, as shown in Figure S4(C).

References

Do Carmo, M. P., 1976. Differential Geometry of Curves and Surfaces. Prentice-Hall, New Jersey.

Fischl, B., Salat, D. H., van der Kouwe, A. J., Makris, N., Segonne, F., Quinn, B. T., Dale, A. M., 2004. Sequence-independent segmentation of magnetic resonance images. NeuroImage 23 (Suppl 1), S69–S84.

Jezzard, P., Balaban, R. S., 1995. Correction for geometric distortion in echo planar images from B0 field variations. Magn Reson Med 34 (1), 65–73.

Jovicich, J., Czanner, S., Greve, D., Haley, E., van der Kouwe, A., Gollub, R., Kennedy, D., Schmitt, F., Brown, G., Macfall, J., Fischl, B., Dale, A., 2006. Reliability in multi-site structural MRI studies: effects of gradient non-linearity correction on phantom and human data. NeuroImage 30 (2), 436–443.